Microwave cavity perturbation of nitrogen doped nano-crystalline diamond films

Jerome A. Cuenca [a, *], Kamatchi Jothiramalingam Sankaran [b, c], Paulius Pobedinskas [b, c], Kalpataru Panda [d], I-Nan Lin [e], Adrian Porch [f], Ken Haenen [b, c], Oliver A. Williams [a]

[a] Cardiff School of Physics and Astronomy, Cardiff, Wales, CF24 3AA, UK
[b] Institute for Materials Research (IMO), Hasselt University, 3590, Diepenbeek, Belgium
[c] IMOMEC, IMEC vzw, 3590, Diepenbeek, Belgium
[d] Center for Nanomaterials and Chemical Reactions, Institute for Basic Science (IBS), 34141, Daejeon, Republic of Korea
[e] Department of Physics, Tamkang University, 251 Tamsui, Taiwan, Republic of China
[f] Cardiff School of Engineering, Cardiff, Wales, CF24 3AA, UK

ARTICLE INFO

ABSTRACT

Non-contact and non-destructive electrical conductivity measurements of nitrogen doped nano-crystalline diamond films have been demonstrated using a microwave cavity perturbation system. The conductivity of the films was controlled by simply varying the CH_4 gas concentration during microwave plasma assisted chemical vapour deposition, thereby promoting the formation of sp^2 carbon at the grain boundaries. The presence of sp^2 carbon is verified through Raman spectroscopy, x-ray photoelectron spectroscopy and electron energy loss spectroscopy, while scanning electron microscopy confirms an increasing surface area for sp^2 to form. The microwave cavity perturbation results show that the measured cavity quality factor varies with CH_4 concentration. The extraction of conductivity is achieved through a depolarisation model, which must be considered when the sample is smaller than the cavity and through both electric and magnetic field perturbations. The microwave measurements are comparable to contacting and damaging measurements when the film conductivity is greater than the substrate, thus demonstrating an invaluable method for determining conductivity without the need for depositing any electrodes on the film.

1. Introduction

Diamond films produced using microwave plasma chemical vapour deposition (MPCVD) are of great interest for a wide variety applications including but not limited to micro-electromechanical systems (MEMS) [1], electrodes [2], thermal management [3,4], terahertz applications [5] and optical windows [6]. All of these applications depend heavily upon a resultant diamond film with a low density of defects; in the case of thermal transport, the benefit of diamond's superior thermal conductivity is hindered by thermal barriers from defects at the nucleation region [7]. This includes the formation of non-diamond carbon at the grain boundaries during growth, namely sp^2 and amorphous carbon. In terms of the dielectric properties, the loss tangent at high frequencies becomes large as well as the low frequency conductivity. The density of non-diamond carbon impurities can be reduced by lowering the CH_4 concentration whilst increasing the microwave power [8,9].

While the sp^2 carbon by-product is an obvious limitation for the above low defect diamond applications, diamond incorporated with electrically conducting impurities has demonstrated potential in others [10]. Electrically conducting diamond may be achieved through doping such as boron or phosphorus by respectively adding trimethylboron or phosphine to the gas phase [11—13] or by increasing the surface sp^2 carbon concentration by increasing the CH_4 concentration to create nano-crystalline diamond (NCD) films. It is also well-known that incorporating N_2 to the CH_4 and H_2 gas mixture influences the electrical conductivity; for NCD films, nitrogen is preferentially incorporated at the grain boundaries resulting in bond distortions, an increase in sp^2 bonding and thus an increase in conductivity [14—18], while earlier reports of polycrystalline diamond (PCD) films deposited using different gases show that N_2 addition actually decreases the electrical conductivity

[19]. Electrically conducting diamond films through doping improves the prospect of MEMS devices [1], negates the need for metal contacts for x-ray beam intensity monitors that introduce additional unwanted absorption edges [14,20], and improves diamond medical implants without ceramic or titanium leads offering lighter and smaller components with a lower risk of failure [21,22]. Conducting NCD films with an abundance of sp^2 carbon, where sp^3 carbon has been partially or completely transformed, have been demonstrated in electron field emission applications [23—25].

Thus, characterising the extent to which an NCD film is electrically conducting is of general importance for furthering various NCD film applications. With the exception of *n* or *p* type doping, the electrical conductivity may be inferred by characterising sp^2 carbon, commonly achieved through Raman spectroscopy, electron energy loss spectroscopy (EELS) and x-ray photoelectron spectroscopy (XPS). All of these techniques are non-contact and offer fingerprint analysis of a small section of the film. Ultimately, a direct electrical measurement is required, where metallic electrodes need to be brought into contact with the film after growth [26]. At optimising the experimental stage, the assessment of multiple samples grown at various conditions is limited by the additional errors associated with the contacting electrodes.

A technique which combines both the non-contacting nature of spectroscopy and a measurement of the electrical properties is through microwave dielectric spectroscopy. While microwaves are generally associated with rapid and efficient heating, dielectric measurements are conducted with much less power and are therefore much less damaging, especially for small samples of low heat capacity. Other techniques, such as those requiring lasers, are prone to heating which is not the case for microwaves which dissipate less than 1 mW in the sample. Currently, one of the most well-known microwave techniques used for examining charge conduction in diamond films is the time resolved microwave conductivity (TRMC) method. This technique uses a microwave waveguide cavity in conjunction with a calibrated light source [27,28]. The sample is placed inside the cavity and upon irradiation, perturbs the frequency response which is a fast transient (<1 μs) associated with light induced conductivity. Notably, Torrealba et al. demonstrated photo-conductivity in PCD films which were otherwise insulating at room temperature. Thus, activated charge transport can be measured with TRMC in semiconducting films. In conventional setups, the reflection coefficient infers the cavity frequency response, however, requires strict calibration to remove standing waves along the transmission line to the cavity. Also, the cavity coupling needs to be adjusted for each sample to maximise the sensitivity.

For electrically conducting NCD films at room temperature, we demonstrate in this work that determining the resistivity using a non-contacting microwave approach does not require a light source, nor the capability to resolve fast transients. In this work, we simply propose the use of microwave cavity perturbation (MCP), all within the frequency domain, to infer the electrical conductivity, minimising the complexity of the system to just a vector network analyser (VNA) and a cavity. In addition, we use a 2-port transmission system with no need to retune owing to the weak coupling antennas, minimising the effects of coupling on the measurement. The caveat here is that the dynamic range of the VNA must be significant to measure low Q factors. In MCP, the empty and sample perturbed frequency responses are measured and the difference is related to the complex dielectric or magnetic properties. MCP has been a popular choice for characterising electrically conducting impurities in diamond samples due to the non-contact setup and significant dielectric contrast between sp^3 and sp^2 carbon in the microwave frequency range [29—31]. While previous studies have been effective for particles, in this work we adopt these systems towards NCD films which introduces a number of challenges.

The first consideration is that MCP requires the sample holder, or in this case the growth substrate, to have a low complex permittivity. In most cases, the sample holder or substrate generally has a low volume and dielectric constant and loss tangent compared to the sample such as quartz. However, for NCD films synthesised using MPCVD, this is the opposite where the substrate is typically significantly larger in volume than the film as to avoid delamination caused by thermal stress and the electrical conductivity of the substrate is commonly significant, such as doped *n* or *p*-type silicon [32]. In this instance, the perturbation is focused on the substrate which determines the lower conductivity detection limit. This detection limit may be improved by changing to a lower conductivity substrate such as quartz or sapphire [27], however, forming stable carbides on these structures is considerably more challenging in addition to the differences in thermal expansion coefficients resulting in delamination upon cooling from elevated temperatures [33].

Suffice to say, in the interest of examining defects and *trace* sp^2 carbon in MPCVD produced NCD films for the aforementioned applications, using MCP is almost futile with a highly conducting substrate. However, for doped diamond film applications, if the conductivity increases significantly such that the conductivity is equivalent to or much larger than that of the substrate, then MCP is of great benefit through non-contact probing of electrical properties. This may be achieved through both electric (*E*) and magnetic (*H*) field perturbations. In which case, in this study we focus on NCD films suitable for conducting diamond film applications.

This paper demonstrates measuring the microwave conductivity of NCD films with a simple rectangular resonator. In Section 2 we discuss the depolarisation model for measuring films since the sample geometries are smaller than the cavity. In Section 3 we present COMSOL Multiphysics® simulations of the cavity and compare this to the analytical models. In Section 4 we have produced representative conducting NCD films by varying the sp^2 carbon content. This has been achieved by varying the CH_4 concentration during MPCVD growth. Finally, in Section 5 we have characterised the films using common spectroscopy methods and have compared this with MCP.

2. Theory

2.1. First order cavity perturbation

MCP is a technique where a sample is placed in the anti-node of a microwave cavity resonator and the observed change in the complex frequency response allows extraction of the complex relative permittivity or permeability. Differences in Q factor have been reported for nanodiamond powders treated in various atmospheres owing to varying sp^2 concentrations [29—31,34]. These studies have all been conducted in the first order scenario, where the E and H-field distribution with and without the sample is similar and so minimal macroscopic depolarisation applies. A simplification is made to the following general cavity perturbation equation [35]:

$$-\frac{\Delta f^*}{f_0} \approx \frac{\int\limits^{V_s} \left[(\mu_r^* - 1)\mu_0 H_s \cdot H_0^* + (\varepsilon_r^* - 1)\varepsilon_0 E_s \cdot E_0^* \right] dV}{\int\limits^{V_c} \left[\mu_0 H_0 \cdot H_0^* + \varepsilon_0 E_0 \cdot E_0^* \right] dV} \quad (1)$$

where $\Delta f^*/f_0$ is the fractional change in complex resonance caused by the perturbation which is defined as $[f_s - f_0]/f_0 + j\frac{1}{2}[1/Q_s -$

$1/Q_0$], f is the resonant frequency, Q is the -3 dB quality factor, μ_0 and ε_0 are the free-space permeability and permittivity respectively, E and H are the electric and magnetic field distributions, respectively, 0 and s denote the unperturbed and perturbed values, V_s and V_c denote the volume of the sample and cavity, respectively, μ_r^* is the complex relative permeability and ε_r^* is the complex relative permittivity of the sample with some dielectric loss from conductivity:

$$\varepsilon_r^* = \varepsilon_{r,1} - j\varepsilon_{r,2} = \varepsilon_{r,1} - j\frac{\sigma_{dc}}{2\pi f\varepsilon_0} \tag{2}$$

where σ_{dc} is the dc conductivity. For a dielectric E-field perturbation with minimal change to the field distribution, this of course simplifies to the well-known first order cavity perturbation equation:

$$-\frac{\Delta f^*}{f_e} \approx (\varepsilon_r^* - 1)\frac{V_s}{2V_m} \tag{3}$$

where V_m is the mode volume or the effective volume over which the electrical energy is stored and e denotes an E-field perturbation.

2.2. Cavity perturbation with depolarisation

For (3) to be valid, $E_0 \approx E_s$ and so sample surfaces should not be perpendicular to the applied E-field as to avoid polarisation charges from building up to create an opposing depolarisation field. This reduces the net field inside the sample and also reconfigures the fields within the cavity. For magnetic field perturbations, skin depth may cause screening effects if the geometry is larger than the skin depth. First order cavity perturbation no longer applies in this case as the net field is geometry and conductivity dependent

($E_s \neq E_0$ or $H_s \neq H_0$). This can somewhat be accounted for by assuming that the sample has some depolarising or demagnetisation factor [36]. For an E-field perturbation perturbation:

$$-\frac{\Delta f^*}{f_e} \approx \frac{\varepsilon_r^* - 1}{1 + N(\varepsilon_r^* - 1)}\frac{V_s}{2V_m} \tag{4}$$

where N is the geometric sample depolarising factor which is positive and less than or equal to 1. The determination of N may be modelled analytically or using finite element modelling (FEM). Equation (4) is plotted in Fig. 1 as a function of conductivity and depolarisation ($\varepsilon_{r,1} = 1$) for a typical rectangular resonator. In first order cavity perturbation, $N = 0$ and thus, simply $\Delta f \propto \varepsilon_{r,1}$ and $\Delta[1/Q] \propto \sigma_{dc}$ as in (3). However, when N is finite, both f and Q are convoluted when σ_{dc} changes and the sensitivity decreases dramatically with very high conductivities. In summary, the three primary considerations for measuring conducting films which are smaller than the cavity are:

1. Sensitivity decreases with increasing N.
2. Δf and $\Delta[1/Q]$ are no longer solely, respectively, attributed to $\varepsilon_{r,1}$ and $\varepsilon_{r,2}$ as both change with σ_{dc}.
3. There are two degenerate regions where Q denotes the sample to be either conducting or insulating.

In respect of using Q to infer conductive loss in a material, when there is depolarisation, point 3 is of grave significance especially when samples have a conductivity ranging from 10^0 to 10^3 S/m [37]. As is shown in Fig. 1, a sample with increasing conductivity will first exhibit a decrease in Q followed by an increase back to the cavities unperturbed value. To the observer, no change in Q could be mistaken for a sample with minimal dielectric loss and simply a
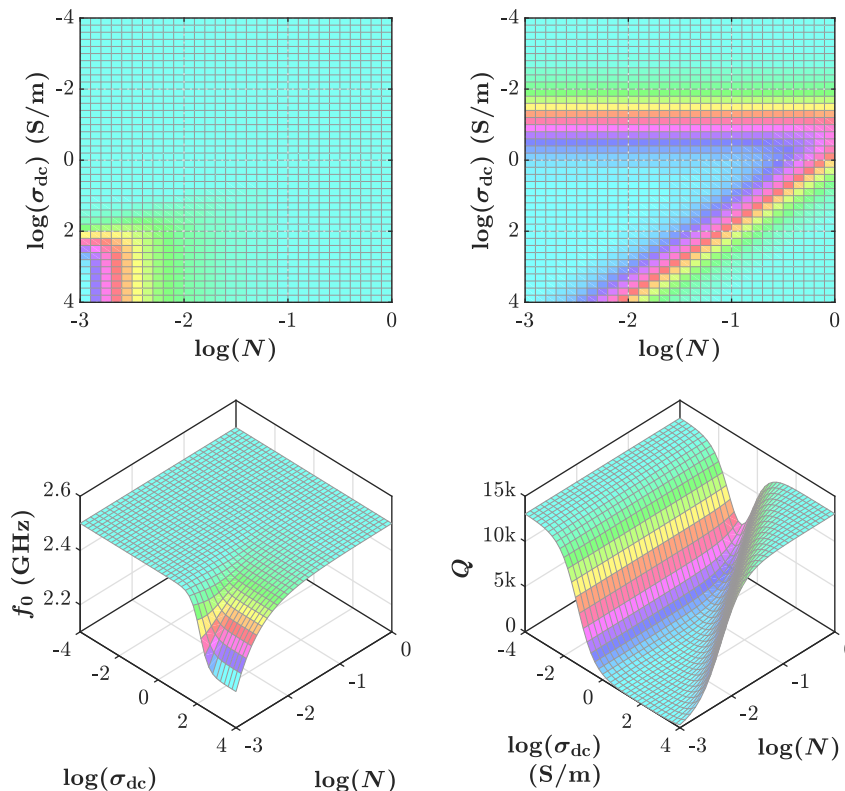

Fig. 1. Frequency (left) and Q factor (right) shift caused by a depolarising $10 \times 10 \times 0.5$ mm sample inside of a $71 \times 60 \times 110$ mm cavity with a mode scaling constant of $V_m/V_c = 0.25$. The initial frequency and Q factor are 2.5 GHz and 13,063, respectively. (A colour version of this figure can be viewed online.)

finite but large dielectric constant such as a material exhibiting Debye like behaviour. This degeneracy issue may be overcome using H-field perturbations assuming of course that $\mu_r^* = 1$ at these frequencies. Any loss caused by a large conductivity is due to the induction of surface currents while a purely dielectric material should not interact with the H-field whatsoever. The screening effect results in a change in the volume of stored energy in the cavity which for the E-field perturbation case results in a decrease in frequency, however in the H-field, this results in a shift upwards [35,38], in which case the perturbation can simply be modelled using (4) except the frequency increases.

3. Finite element model

A rectangular cavity has been modelled in COMSOL Multiphysics® at 2.5 GHz with a typical CVD diamond film substrate, details in Table 1, such that the extremities are within the cavity to cause finite depolarisation $N > 0$. The CVD film is modelled as a 1 μm transition boundary condition on the surface of a $10 \times 10 \times 0.5$ Si substrate (all surfaces except for the base). For the E-field measurement, the film is suspended on a polytetrafluoroethylene (PTFE) sheet that extends through the cavity. The measurement mode used here is the TE_{011} mode in which the E-field standing wave is at a maximum in the centre of the cavity and at a minimum on the cavity walls, shown in Fig. 2a. Conversely, the H-field standing wave is at a local minimum in the centre and a maximum towards the walls of the cavity, shown in Fig. 2b. The dimensions of the cavity are ($61 \times 70 \times 110$ mm) and have been chosen as such to minimise mode overlap caused by degeneracy.

Fig. 2c and d shows the field distribution in the presence of a heavily conducting sample ($\sigma_{dc} = 10^6$ S/m) placed at the maxima of the E and H-fields. Note that in both cases the field screens dramatically and the overall distribution of the mode is changed, especially in the E-field case where the field decays before it reaches the sample, demonstrating that $E_0 \neq E_s$ and ultimately showing that first order cavity perturbation cannot apply.

The associated changes in f and Q for a sample of varying σ_{dc} are shown in Fig. 3. For the E-field perturbation, as stated previously, in the non-depolarising case the frequency should not change for a given conductivity, however, it is clear in Fig. 3a that the frequency decreases with increasing conductivity owing to depolarisation. The simulation was conducted with and without the Si substrate to understand the measurement limitations. Without the Si substrate, the analytical solution (where $N_e = 8.7 \times 10^{-5}$ and $V_m = 0.25 \times V_c$) is in good agreement with the simulation. In Fig. 3b, Q_e decreases and increases accordingly with (4), demonstrating that the analytical model is relatively accurate at describing the change in f and Q factor for the E-field perturbation of a film with a lossless substrate. There is however, a large deviation from the model when the Si substrate is introduced; note that f_e and Q_e decrease to lower initial values for a lower conductivity. The point at which the Si and lossless models meet defines the lower conductivity measurement limit ($\approx 10^3$ S/m), again highlighting that this MCP system is only suitable for measuring conducting NCD films. As the conductivity of

the film increases, the effects of the Si are less prominent. In addition, there is also a slight deviation in f_e but more so in Q_e which is due to the fact that at the sample location the H-field is non-zero and so the material produces a small perturbation into the stray H-field. Normally this perturbation is insignificant for dielectric samples, however, since conducting samples also perturb the H-fields, there is an additional contribution. At this point, it is important to note that one could observe that the degeneracy of Q_e can be corrected by simply checking the E-field frequency shift; if the frequency does not change, we are in the low conductivity region and if it decreases, then the sample has a high conductivity. However, the shifts modelled here do not consider the low but finite dielectric constant of the sample which may change, and so the frequency will always decrease. Therefore, we highlight the importance of performing additional H-field perturbations.

For the H-field perturbation, the deviation from the analytical model (where for fitting purposes only, $N_h = 1.23 \times 10^{-6}$ and $V_m = 500 \times V_c$) is less significant in both f_h and Q_h. Note that the V_m scalar is much larger since the H-field is distributed all around the cavity walls. The introduction of the lossy Si substrate also had minimal impact to the H-field model, although the frequency shift is smaller in the high conductivity region. This is due to a stray perturbation in the E-field. While a low dielectric constant material has little effect on the stray E-field, the sample conductivity may be significant enough to alter the E-field distribution. In addition, the simulated sample here assumes no air gap between the wall and the sample which may also introduce a small shift downwards in f_h (see supplementary information). The conductivity related depolarisation effects which result in H-field screening, and therefore an increase in f, have an onset at a higher conductivity since $N_h < N_e$. In summary, the sample conductivity can be inferred from the following groups, with the observed differences from the unperturbed; f_e has been included although as explained previously its observation is obscured by $\varepsilon_{r,1}$:

1. $0 - 10^2$ S/m - Insulating to lossy dielectric Q_e decreases
2. $10^2 - 10^4$ S/m - Lossy dielectric to semi-conductor Q_e is heavily damped, Q_h decreases and f_e decreases
3. $10^4 - 10^7$ S/m - Semi-conductor to metallic Q_e decreases, Q_h decreases, f_e decreases and f_h increases
4. Greater than 10^7 S/m - Metallic f_e decreases f_h and increases.

4. Experimental method

The MCP system has been tested with NCD films $10 \times 10 \times 0.5$ mm on Si. The substrates used for growth are n-type Si (100) substrates ($10 - 20$ kΩ cm). Prior to the deposition of NCD films, the Si substrates were seeded with a water-based colloidal suspension of ultra dispersed detonation nanodiamond of size $6 - 7$ nm (NanoCarbon Institute Co., Ltd.) via drop casting and subsequent spin-drying [39]. The NCD films were grown on the seeded Si substrates in an ASTeX 6500 series MPCVD reactor. Mixtures of CH_4, H_2 and N_2 were used as the reactant gases for the microwave discharges. While the N_2 was kept constant at 3% (9 sccm), the CH_4 was varied from 1% (3 sccm) to 15% (45 sccm) and complemented by H_2 so as to maintain a 300 sccm of total flow rate. The plasma was induced with a microwave power of 3 kW and a pressure of 65 Torr.

The MCP measurements were carried out using the aluminium rectangular microwave cavity resonator shown in Fig. 4. Two gold plated coaxial SMA ports have been added to the side of the resonator with loop H-field antennas to couple into the TE_{011} mode at approximately 2.5 GHz. The cavity is fabricated into 2 pieces of aluminium and attached together using steel clips. The cavity is
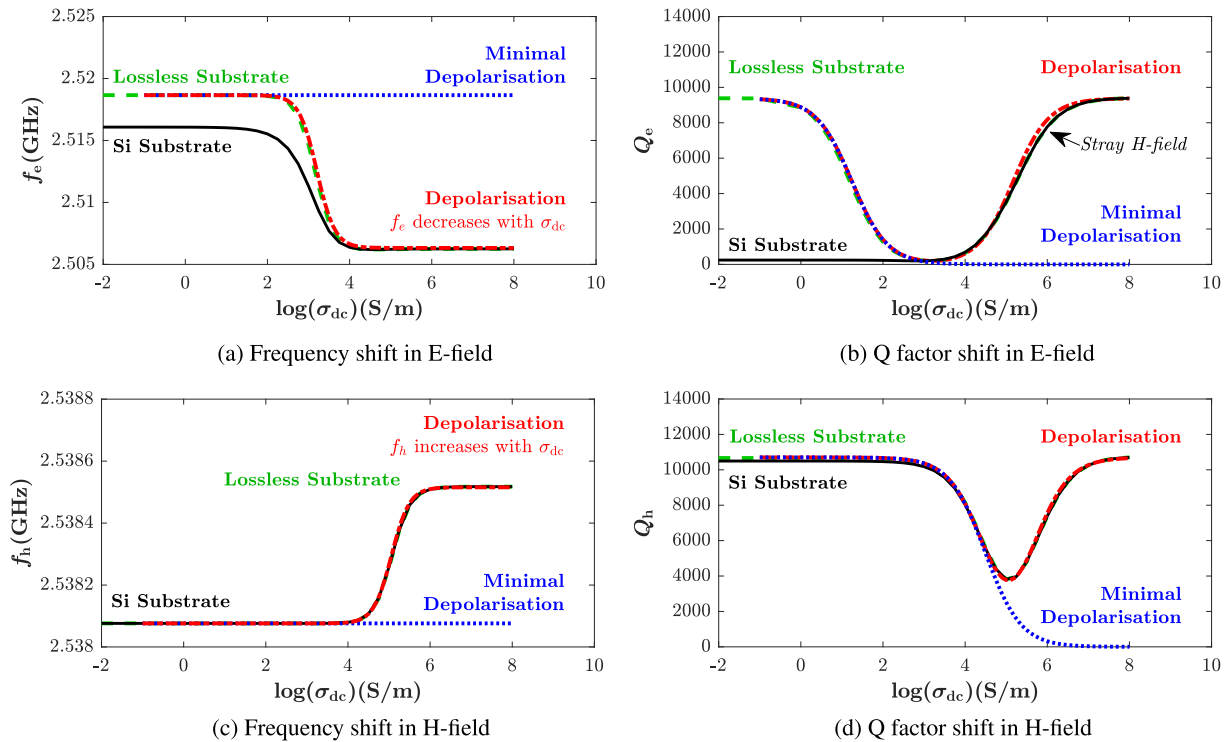
Table 1
COMSOL Multiphysics® parameters.

Cavity Material	Al, $\sigma = 2 \times 10^7$ S/m
Cavity Dimensions:	$61 \times 70 \times 110$ mm
Cavity Frequency (f_0):	2.538 GHz
Cavity Q factor (Q_0)	13,064, PTFE loaded = 9,436
Sample	1 μm thick CVD Diamond, $\varepsilon_{r,1} = 5.7$, $\mu_{r,1} = 1$
Substrate	Si, $\sigma = 10^{0.5}$ S/m, $\varepsilon_{r,1} = 11.7$
Sample Conductivity	$10^{-6 \text{ to } 8}$ S/m
Sample Holder for E-Field	PTFE, $\sigma = 10^{-4}$ S/m, $\varepsilon_{r,1} = 2.1$

(a) E_0

(b) H_0

(c) E_s

(d) H_s
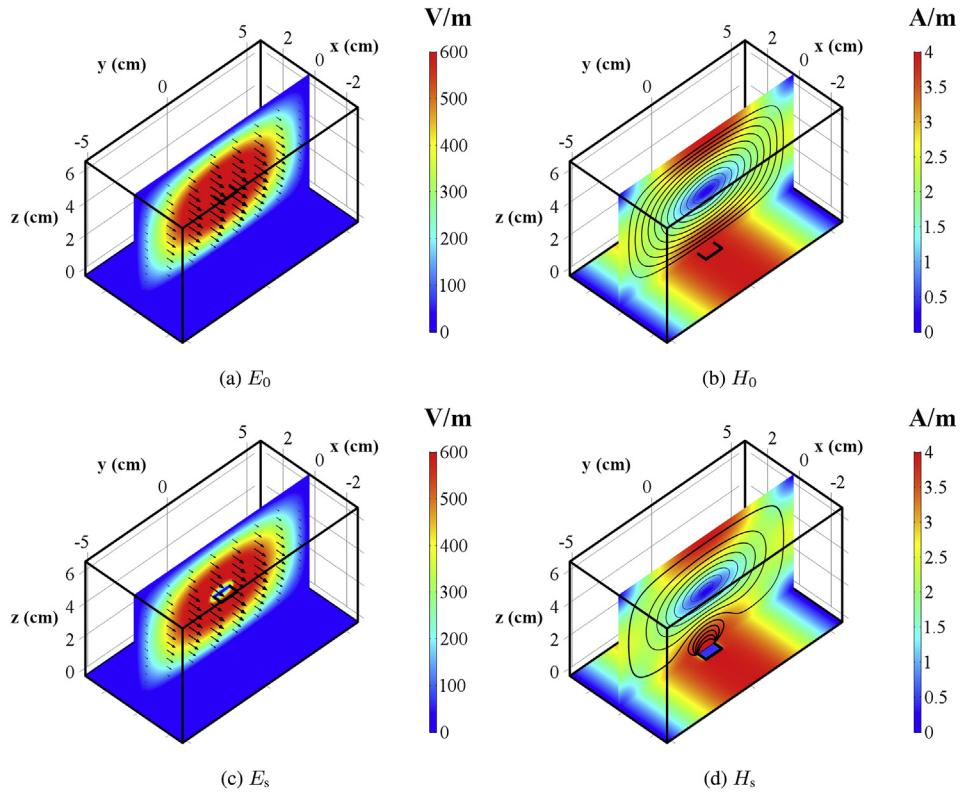
Fig. 2. COMSOL Multiphysics® simulations of the TE$_{011}$ mode at 2.5 GHz. The perturbed fields are for a sample with a film conductivity of 10^6 S/m. (A colour version of this figure can be viewed online.)

(a) Frequency shift in E-field

(b) Q factor shift in E-field

(c) Frequency shift in H-field

(d) Q factor shift in H-field

Fig. 3. FEM results of frequency and Q factor shifts of a substrate of varying film conductivity. The solid and dashed lines are the COMSOL Multiphysics® simulated values with a lossy (eg. Si) and lossless (eg. quartz) substrate respectively. The dotted and dash-dotted lines are the analytical solutions given by 3 and 4 for $V_s = 10 \times 10 \times 0.001$ sample The dotted lines denote the non-depolarising case ($N = 0$), while the dash-dotted lines denote the depolarising case ($N \neq 0$). Deviation from the analytical is due to the loss associated with the lossy substrate and finite perturbation in the opposing stray fields. (A colour version of this figure can be viewed online.)
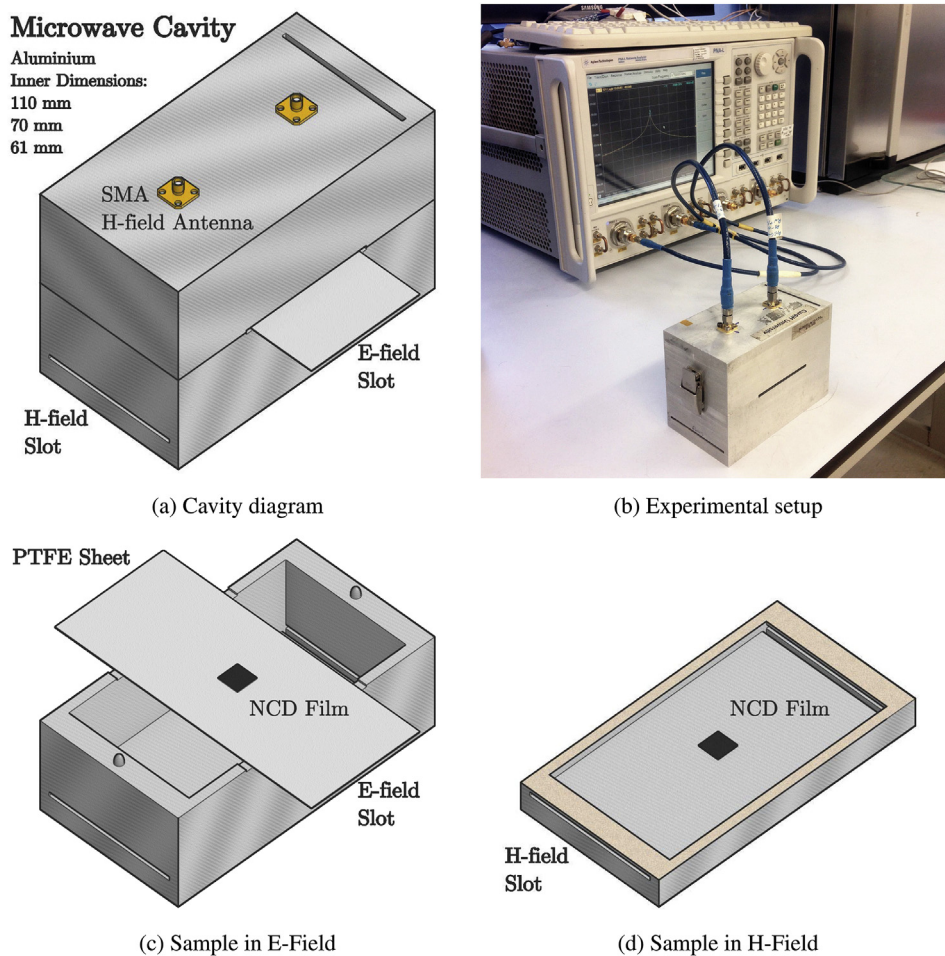
(a) Cavity diagram

(b) Experimental setup

(c) Sample in E-Field

(d) Sample in H-Field

Fig. 4. Schematic of the rectangular resonator used in this study with experimental setup. (A colour version of this figure can be viewed online.)

split into two pieces in such a way that the current distribution of the mode is unaffected; any seams run parallel to the surface currents. In addition, sample slots have been milled for various other sheet sizes. A thin sheet of PTFE is used to suspend the NCD films in the E-Field. The unperturbed response for the E-field measurements is taken as the PTFE loaded cavity while for the H-field measurements, the samples are simply placed on the bottom of the cavity.

The surface morphology and the thicknesses of the NCD films were characterised using a FEI Quanta 200 FEG scanning electron microscope (SEM) operated at 15 kV. The crystalline quality and the bonding structure of the films were examined using a Horiba Jobin Yvon T64000 micro-Raman spectrometer (equipped with a BXFM Olympus 9/128 microscope, a Horiba JY Symphony CCD detector with a 488 nm Lexell SHG laser), X-ray photoelectron spectroscopy (XPS; PHI 1600) and core-loss electron energy loss spectroscopy (EELS, Gatan Enfina) in transmission electron microscopy, respectively.

5. Results and discussion

The SEM micrographs in Fig. 5 show that at low CH_4 concentration, the produced NCD film consists of 0.5—1 micron sized grains. As the CH_4 concentration is increased to 5% however, the observed grain size decreases dramatically, resulting in a much larger surface area to volume ratio, thus an expectation for a much larger volume of surface sp^2 carbon impurities. Increasing the CH_4

concentration to 10% further decreases the grain size while at 15%, the material has formed a 'ridge' like surface morphology, comparable to those found in previous studies of nitrogen doped NCD films [40]. Under an optical microscope, these NCD films get progressively darker, implicit of the increasing non-diamond carbon content. In addition, the increase in CH_4 concentration has increased the growth rate of the films, resulting in a variation in film thickness which will need to be considered in the depolarisation model.
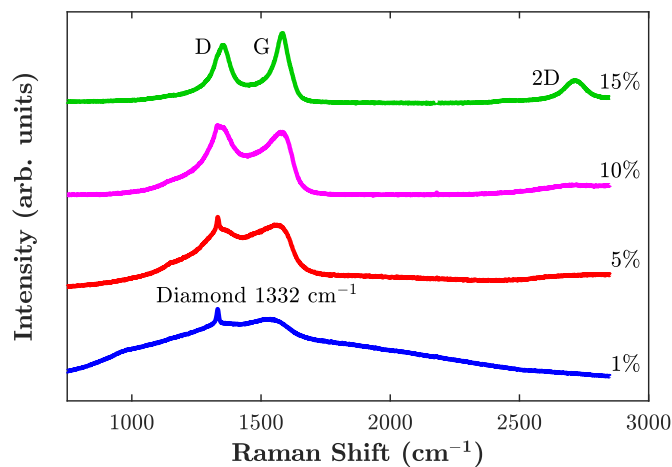
The micro-Raman spectroscopy measurements in Fig. 6 show that at low CH_4 concentration, the characteristic peak at 1332 cm^{-1} indicates the presence of sp^3 carbon. The broad band around this peak (D-band) is generally associated with induced disorder and amorphous carbon [41,42] and the large background to other surface contaminants. The broad band at approximately 1580 cm^{-1} (G band) is associated with significant concentrations of graphitic sp^2 carbon within the film [43]. As the CH_4 concentration increases, the intensity of the diamond peak starts to diminish, with an associated increase in the FWHM. The intensity of the D and G bands start to increase in addition to a decrease in FWHM. This is indicative of the formation of large volumes of sp^2 carbon while the sp^3 carbon significantly decreases. This is also true for 10% and finally at 15% CH_4, where the diamond is practically non-existent and we are left with large concentrations of sp^2 carbon.

The bonding structure of the NCD films was determined by XPS (Fig. 7) and TEM-EELS (Fig. 8). The C1s spectra is sensitive to both sp^3 and sp^2 and the relative abundance can be inferred through

(a) CH$_4$ = 1%   (b) CH$_4$ = 5%

(c) CH$_4$ = 10%   (d) CH$_4$ = 15%
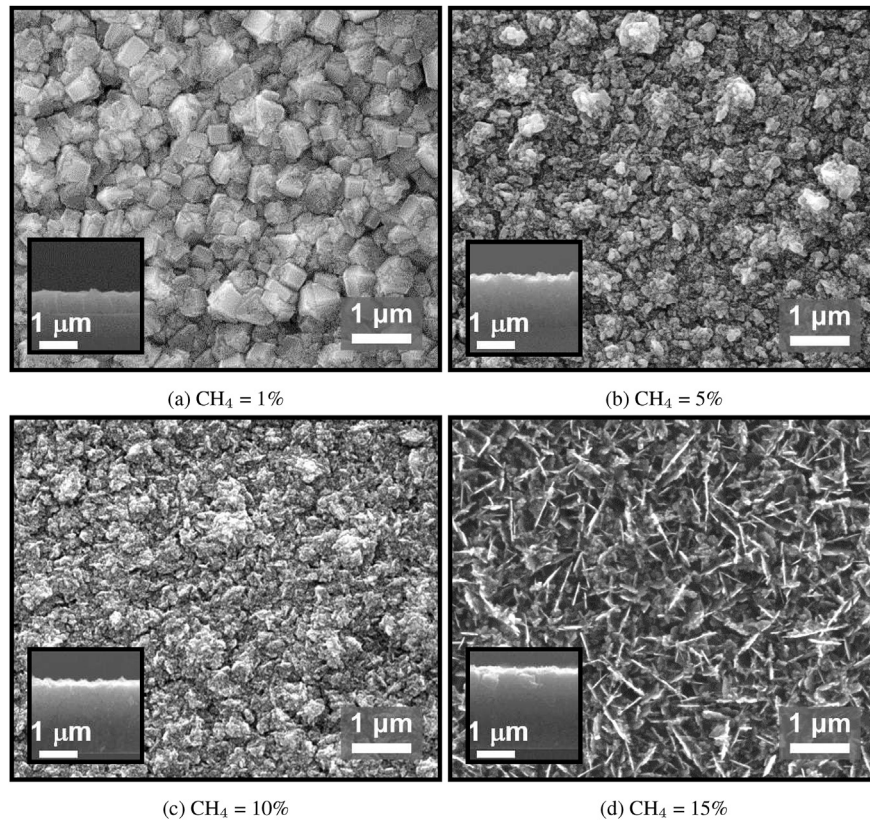
Fig. 5. SEM micrographs of nitrogen doped NCD films as a function of CH$_4$ concentration. The grain size reduces with increasing CH$_4$ concentration. The inset cross-section of the films shows a small variation in film thickness.

deconvolution of the two characteristic peaks, where the sp^3 peak is typically observed at a higher binding of ca. 285 eV than the sp^2 peak at ca. 284 eV [44,45]. In this case, the FWHM and centre of the fitted Gaussian peaks have been fixed, however, sample charging may shift the whole spectra, a limitation of characterising sp^2 and sp^3 carbon in this way. This is clearly the case for the 10% sample. The sp^2 peak can be inferred from the sample grown at the highest CH$_4$ concentration of 15%, where it was previously identified through micro-Raman spectroscopy that minimal sp^3 carbon is

present. The sp^2 peak is identified at ca. 285.1 eV. As the CH$_4$ concentration is reduced, the whole spectra shifts slightly to higher binding energies, owing to the growth of the sp^3 peak. This peak is identified at ca. 284.8 eV, with additional broad peaks at binding energies > 285 eV, associated with various surface contaminations such as C-O and C-H groups [44]. This latter feature is observed in all of the samples with the most prominent peak shown in the lowest CH$_4$ concentration, congruent with the large background


Fig. 6. Micro-Raman spectroscopy (488 nm) of nitrogen doped NCD films as a function of CH$_4$ concentration. The 1332 cm^{-1} peak is associated with sp^3 carbon, while the D and G bands with sp^2 carbon. (A colour version of this figure can be viewed online.)
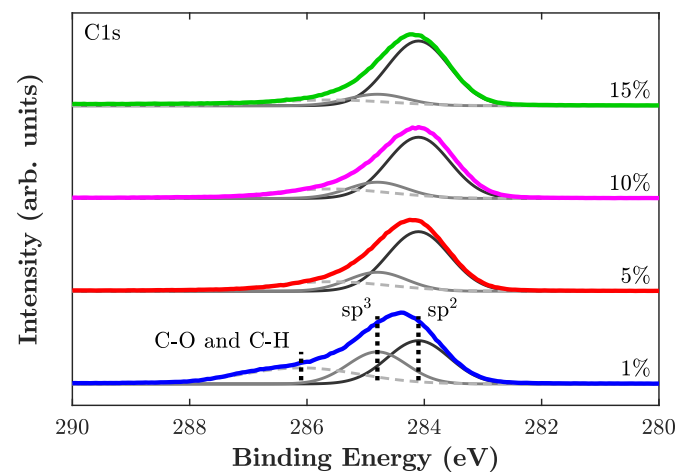
Fig. 7. XPS C1s spectra of nitrogen doped NCD films. Three main peaks at ca. 284.1, 284.8 and > 285 eV are attributed, to sp^2 carbon, sp^3 carbon and C-O and C-H bonds of surface contamination, respectively. (A colour version of this figure can be viewed online.)
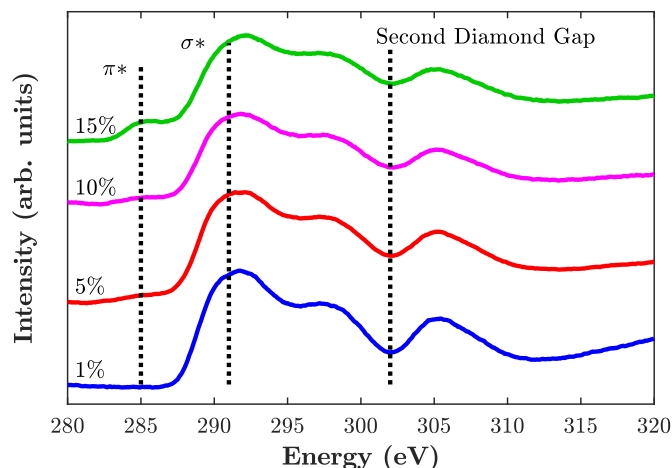
Fig. 8. Core loss EELS spectra of nitrogen doped NCD films with varying CH_4 concentration. The edge at 291 eV is associated with 1s→σ* transitions of sp^2 and sp^3 carbon while the peak at 285 eV is associated with 1s→π* transitions for sp^2 carbon. (A colour version of this figure can be viewed online.)

found in the 1% CH_4 sample measured in the micro-Raman Spectroscopy measurements.

For EELS, the sp^2: sp^3 ratio can be inferred by the π^* and σ^* resonances, where the former is solely related to sp^2 and the latter to both sp^3 and sp^2 carbon [46]. The C1s spectra in Fig. 8 shows a characteristic π^* peak at 285 eV in the 15% sample, indicative of surface sp^2 carbon. This peak is due to C1s electrons transitioning to the π^* orbitals [46]. In addition, the σ^* edge, which is both implicit of sp^3 and sp^2 carbon, is found at ca. 291 eV. This feature, in addition to the dip at ca. 302 eV known as the second diamond gap [46], implies the presence of sp^3 carbon. As the CH_4 concentration decreases, the π^* peak becomes less prominent and the second diamond gap minimum decreases, showing that sp^2 carbon decreases and sp^3 carbon increases as expected with decreasing CH_4 concentration.

The MCP measurements shown in Fig. 9 and tabulated in Table 2 show that the perturbation caused by the high resistivity Si substrate is significant such that Q_e is heavily loaded from 9326 to 250 while Q_h is relatively unchanged. In addition, f_h did not increase and hence the skin depth is still larger than the sample thickness and so the conductivity of the substrate is not metallic. This perturbation is caused by the conducting properties of the Si and strongly implies that we are operating near the depolarisation limit. The large decrease in Q_e, marginal decrease in f_h and Q_h implies that the conductivity of the Si substrate is approximately $10^{0.6}$ S/m. The marginal decrease in f_h is unexpected however, since the FEM model and the analytical model given in (4) do not predict any decrease in f_h. The reason for this is actually due to a finite gap between the sample and the cavity wall, which produces an additional depolarisation and stray field effect (verified through an additional FEM model, see supplementary information). This slightly increases the σ_{dc} onset of screening effects, where f_h increases. This does not affect the overall conclusions of the work, as the Q_h measurements simply follow the minimal depolarisation curve to a slightly larger onset conductivity.

For the NCD film produced at a CH_4 concentration of 1%, Fig. 9 shows that Q_e decreases to less than that of the Si substrate and the downward shift in f_e is less than the Si substrate. This may imply an increase in conductivity and a decrease in dielectric constant. However, this may also just be a sign of a decrease in conductivity, impossible to determine in the absence of H-field measurements when operating near the depolarisation limit.

(a) E-Field

(b) H-Field
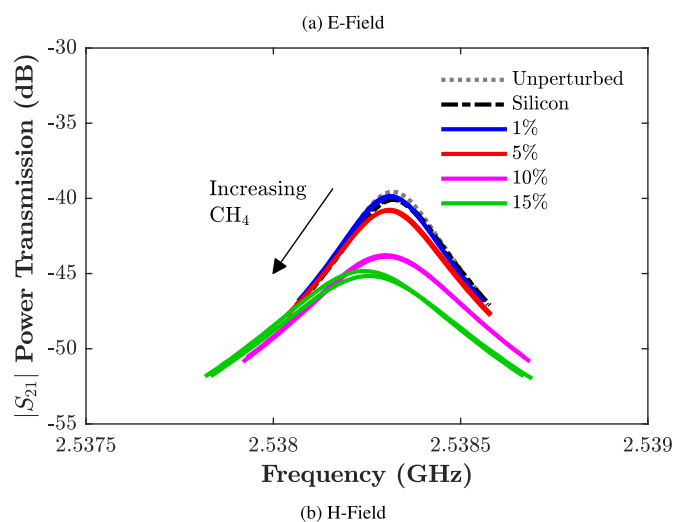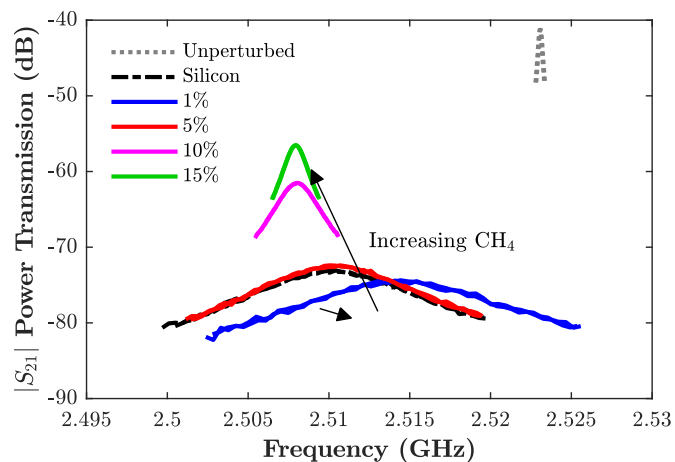
Fig. 9. MCP measurements of NCD films as a function of CH_4 concentration (2 separate measurements of each). Unperturbed measurement consists of a PTFE sheet suspended in the centre of the cavity for E-field while the sample is placed at the bottom of the cavity for the H-field. (A colour version of this figure can be viewed online.)

With the additional MCP H-field measurement, Q_h for the 1% sample does not decrease as much as the Si substrate, meaning that the conductivity actually decreases compared to the bare Si. This implies that when diamond is deposited onto the Si substrate, it actually *decreases* the conductivity of the whole substrate which could be described by a decrease in surface conductivity of the Si substrate caused by the diamond layer. Thereafter, the increase in CH_4 concentration results in an increase in Q_e and a decrease in Q_h, meaning that the conductivity increases. Even at the largest CH_4 concentrations, the conductivity never exceeds the value where the skin depth is smaller than the NCD film thickness such that the H-field perturbation increases in frequency.

Since the degeneracy has been solved for the MCP Q factor measurements, the conductivity of the NCD films can be calculated with results given in Table 2 and plotted onto the analytical and FEM model in Fig. 10. While an approximate value of conductivity can be estimated by assuming all films to have a 1 μm thickness, since the thickness is known from the SEM cross-section micrographs in Fig. 5, a more accurate value can be estimated. For each thickness, the model needs to be adjusted accordingly for each sample as is shown in Fig. 10. With increasing thickness, the whole model is shifted to lower conductivities. The conductivity of the NCD films calculated from the MCP method increases from

Table 2
MCP Q factor with standard deviations taken for 2 sample measurements.

Sample	Q_e	Q_h	σ_{mcp} (S/m)	σ_{dc}[a] (S/m)	Thickness (μm)
Empty[b]	9326±2	10583±16	0	—	—
Si	250±1	9953±7	$10^{0.6}$	$10^{-1.3 \text{ to } -0.8}$	500
1%	210±2	10308±4	$10^{3.2}$ [c]	—	0.6
5%	272±1	9310±11	$10^{3.5}$	$10^{2.9 \text{ to } 3}$	1.4
10%	983±2	6636±28	10^{4}	$10^{3.6 \text{ to } 3.7}$	1.9
15%	1748±3	5843±190	$10^{4.1}$	$10^{3.8 \text{ to } 3.9}$	2.0

[a] Estimated with a multi-meter contacting the film, $\sigma_{dc} \approx \text{length}/(\text{thickness} \times \text{width} \times \text{resistance})$.
[b] Q_e is the PTFE loaded cavity while Q_h is the empty cavity.
[c] Erroneous, measurement approaches the limit of 10^3 S/m.

approximately 10^3 to 10^4 S/m.

The increase in conductivity may simply be explained by the volume increase in sp^2 carbon. From the SEM micrographs, it is clear that the surface area of the films is increasing with CH_4 concentration, which further increases the volume of surface impurities. Additionally, the Raman, XPS and EELS measurements, identify these impurities as sp^2 carbon which is electrically conducting. This is congruent with nanodiamond studies of varying particle size [34], although in this instance it is the film grain size varying. Based on this study, the expectation is that the Q factor would decrease with sp^2, however, the complete opposite is observed in Fig. 9, highlighting the importance of considering depolarisation, and H-field measurements in determining the conductivity using MCP. The absolute values of conductivity in Table 2, are corroborated with the rough estimations of

conductivity using two point measurements. A significant variation in the measured value was, however, found whilst using the multi-meter, which explains the discrepancy between the two measurements.

Another important observation is that the MCP measurement of the 1% sample is not correct as an extremely large resistance was measured using the multi-meter. The inability to measure a precise resistance demonstrates that there is a heavily insulating diamond film on the Si substrate and so the results presented for 1% are erroneous. The measured MCP value is merely a variation in the conductivity of the Si after it has been grown on. This highlights the biggest consideration for the MCP measurement system for NCD films in that MCP can only measure the conductivity of the films if it is greater than the substrate. As the CH_4 concentration increases along with the conductivity, however, MCP becomes focused on the film as opposed to the substrate.
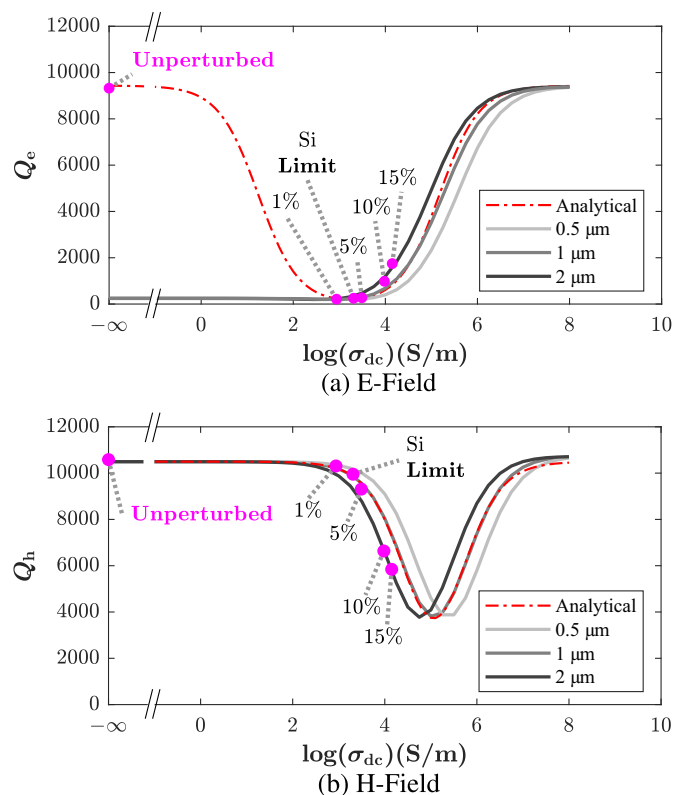
6. Conclusion

While not nearly as sensitive as powder systems presented in previous studies, an MCP system has been demonstrated as a non-contacting probe for fast and non-invasive evaluation of the electrical conductivity of nitrogen doped NCD films. It is clear that the lower measurement limit in conductivity is determined by the microwave dielectric properties of the sample substrate and with most CVD growth applications reliant on Si, limits the use of MCP in evaluating conducting impurities. It is however, extremely useful for diamond applications which require the film to reach conductivities of greater than around 10^3 S/m. The finite depolarisation caused by a small sample introduces a degeneracy in the Q-factor measurements, whereby one must exercise caution relating Q factor to conductivity. In this instance, it is not true to simply state that the sample with the highest conductivity exhibits the lower Q factor, as is the case for the simplified cavity perturbation equations.

Hence, MCP conducted using a rectangular cavity is generally only useful for examining *electrically conducting* NCD films that greatly exceeds the conductivity of the substrate. For the examination of NCD films grown with nitrogen doping, with aim of synthesising sp^3 carbon needles encased in sp^2 carbon for emission applications or for boron doping of diamond, MCP is extremely valuable for quickly determining how growth parameters (such as power, pressure, dopant concentration etc.) affect the overall electrical conductivity of the film without damaging the film in anyway.

Fig. 10. MCP Q factor measurements plotted against the depolarisation model. The dot-dashed lines show the analytical depolarisation model whereas the solid lines show COMSOL Multiphysics® models of varying thickness. For visibility and demonstration of the thickness effect, the thickness lines for each sample as is given in Table 2 are not plotted but rather 0.5, 1 and 2 μm. (A colour version of this figure can be viewed online.)

12I8416N and 1519817N, and the Methusalem "NANO network. The Hercules Foundation Flanders is also acknowledged for financial support of the Raman equipment. J. A. Cuenca is an EPSRC Post-doctoral researcher and K. J. S and P. P are Postdoctoral Fellows of the Research Foundation-Flanders (FWO).

Appendix A. Supplementary data

Supplementary data to this article can be found online at https://doi.org/10.1016/j.carbon.2018.12.025. Information on the data presented here, including how to access them, is available from the Cardiff University data catalogue at http://doi.org/10.17035/d.2018.0065733586.

References

[1] F. Buja, A.V. Sumant, J. Kokorian, W.M. Van Spengen, Electrically conducting ultrananocrystalline diamond for the development of a next generation of micro-actuators, Sens. Actuators, A 214 (2014) 259–266, https://doi.org/10.1016/j.sna.2014.04.042. https://doi.org/10.1016/j.sna.2014.04.042.

[2] Q. Zhang, Y. Liu, S. Chen, X. Quan, H. Yu, Nitrogen-doped diamond electrode shows high performance for electrochemical reduction of nitrobenzene, J. Hazard Mater. 265 (2014) 185–190, https://doi.org/10.1016/j.jhazmat.2013.11.065. https://doi.org/10.1016/j.jhazmat.2013.11.065.

[3] F.N. Faili, C. Engdahl, E. Francis, GaN-on-Diamond substrates for HEMT applications, Diamond Tooling Journal 1 (2009) 52–55.

[4] F. Ejeckam, D. Francis, F. Faili, D. Twitchen, B. Bolliger, D. Babic, J. Felbinger, GaN-on-diamond: a brief history, in: Lester Eastman Conference on High Performance Devices, LEC), 2014, pp. 1–5, https://doi.org/10.1109/LEC.2014.6951556.

[5] M.Q. Ding, L. Li, Y. Du, X. Wu, J. Cai, J. Feng, Development of an extremely thin-diamond window for terahertz traveling wave tubes, Diam. Relat. Mater. 79 (September) (2017) 173–178, https://doi.org/10.1016/j.diamond.2017.09.015. https://doi.org/10.1016/j.diamond.2017.09.015.

[6] F. Mazzocchi, S. Schreck, D. Strauss, G. Aiello, A. Meier, T. Scherer, Diamond windows diagnostics for fusion reactorsâĂŤUpdates of the design, Fusion Eng. Des. 123 (2017) 820–824, https://doi.org/10.1016/j.fusengdes.2017.04.012. https://doi.org/10.1016/j.fusengdes.2017.04.012.

[7] H. Sun, R.B. Simon, J.W. Pomeroy, D. Francis, F. Faili, D.J. Twitchen, M. Kuball, Reducing GaN-on-diamond interfacial thermal resistance for high power transistor applications, Appl. Phys. Lett. 106 (11) (2015) 111906, https://doi.org/10.1063/1.4913430.

[8] H. Windischmann, G.F. Epps, Free-standing diamond membranes: optical, morphological and mechanical properties, Diam. Relat. Mater. 1 (5–6) (1992) 656–664, https://doi.org/10.1016/0925-9635(92)90185-Q.

[9] O.A. Williams, Nanocrystalline diamond, Diam. Relat. Mater. 20 (5–6) (2011) 621–640, https://doi.org/10.1016/j.diamond.2011.02.015. arXiv:0704.0701. https://doi.org/10.1016/j.diamond.2011.02.015.

[10] M. Mertens, I.-N. Lin, D. Manoharan, A. Moeinian, K. Brühne, H.J. Fecht, Structural properties of highly conductive ultra-nanocrystalline diamond films grown by hot-filament CVD, AIP Adv. 7 (1) (2017) 015312, https://doi.org/10.1063/1.4975226. http://aip.scitation.org/doi/10.1063/1.4975226.

[11] W. Gajewski, P. Achatz, O.A. Williams, K. Haenen, E. Bustarret, M. Stutzmann, J.A. Garrido, Electronic and optical properties of boron-doped nanocrystalline diamond films, Phys. Rev. B Condens. Matter 79 (4) (2009) 1–14, https://doi.org/10.1103/PhysRevB.79.045206.

[12] T. Teraji, K. Arima, H. Wada, T. Ito, High-quality boron-doped homoepitaxial diamond grown by high-power microwave-plasma chemical-vapor deposition, J. Appl. Phys. 96 (10) (2004) 5906–5908, https://doi.org/10.1063/1.1805180.

[13] W. Janssen, S. Turner, G. Sakr, F. Jomard, J. Barjon, G. Degutis, Y.G. Lu, J. D'Haen, A. Hardy, M.V. Bael, J. Verbeeck, G.V. Tendeloo, K. Haenen, Substitutional phosphorus incorporation in nanocrystalline CVD diamond thin films, Phys. Status Solidi Rapid Res. Lett. 8 (8) (2014) 705–709, https://doi.org/10.1002/pssr.201409235.

[14] M. Zou, M. Gaowei, T. Zhou, A.V. Sumant, C. Jaye, D.A. Fisher, J. Bohon, J. Smedley, E.M. Muller, An all-diamond X-ray position and flux monitor using nitrogen-incorporated ultra-nanocrystalline diamond contacts, J. Synchrotron Radiat. 25 (4) (2018) 1060–1067, https://doi.org/10.1107/S1600577518006318.

[15] P. Achatz, O.A. Williams, P. Bruno, D.M. Gruen, J.A. Garrido, M. Stutzmann, Effect of nitrogen on the electronic properties of ultrananocrystalline diamond thin films grown on quartz and diamond substrates, Phys. Rev. B Condens. Matter 74 (15) (2006) 3–9, https://doi.org/10.1103/PhysRevB.74.155429.

[16] A.I. Shames, A.M. Panich, S. Porro, M. Rovere, S. Musso, A. Tagliaferro, M.V. Baidakova, V.Y. Osipov, A.Y. Vul, T. Enoki, M. Takahashi, E. Osawa, O.A. Williams, P. Bruno, D.M. Gruen, Defects localization and nature in bulk and thin film utrananocrystalline diamond, Diam. Relat. Mater. 16 (10) (2007) 1806–1812, https://doi.org/10.1016/j.diamond.2007.08.026.

[17] S. Dunst, H. Sternschulte, M. Schreck, Growth rate enhancement by nitrogen in diamond chemical vapor deposition-a catalytic effect, Appl. Phys. Lett. 94 (22) (2009) 1–4, https://doi.org/10.1063/1.3143631.

[18] T. Ikeda, K. Teii, C. Casiraghi, J. Robertson, A.C. Ferrari, Effect of the sp^2 carbon phase on n-type conduction in nanodiamond films, J. Appl. Phys. 104 (7) (2008) 1–7, https://doi.org/10.1063/1.2990061.

[19] V. Baranauskas, B.B. Li, A. Peterlevitz, M.C. Tosin, S.F. Durrant, Nitrogen-doped diamond films, J. Appl. Phys. 85 (10) (1999) 7455–7458, https://doi.org/10.1063/1.369378.

[20] K. Kummer, A. Fondacaro, F. Yakhou-Harris, V. Sessi, P. Pobedinskas, S.D. Janssens, K. Haenen, O.A. Williams, J. Hees, N.B. Brookes, Thin conductive diamond films as beam intensity monitors for soft x-ray beamlines, Rev. Sci. Instrum. 84 (3) (2013) 035105, https://doi.org/10.1063/1.4794439.

[21] K. Ganesan, D.J. Garrett, A. Ahnood, M.N. Shivdasani, W. Tong, A.M. Turnley, K. Fox, H. Meffin, S. Prawer, An all-diamond, hermetic electrical feedthrough array for a retinal prosthesis, Biomaterials 35 (3) (2014) 908–915, https://doi.org/10.1016/j.biomaterials.2013.10.040.

[22] P.A. Nistor, P.W. May, Diamond thin films: giving biomedical applications a new shine, J. R. Soc. Interface 14 (134) (2017) 1–14, https://doi.org/10.1098/rsif.2017.0382.

[23] S. Deshmukh, K.J. Sankaran, K. Srinivasu, S. Korneychuk, D. Banerjee, A. Barman, G. Bhattacharya, D.M. Phase, M. Gupta, J. Verbeeck, K.C. Leou, I.N. Lin, K. Haenen, S.S. Roy, Local probing of the enhanced field electron emission of vertically aligned nitrogen-doped diamond nanorods and their plasma illumination properties, Diam. Relat. Mater. 83 (February) (2018) 118–125, https://doi.org/10.1016/j.diamond.2018.02.005. https://doi.org/10.1016/j.diamond.2018.02.005.

[24] R. Rameneti, K.J. Sankaran, S. Korneychuk, C.J. Yeh, G. Degutis, K.C. Leou, J. Verbeeck, M.K. Van Bael, I.N. Lin, K. Haenen, Vertically aligned diamond-graphite hybrid nanorod arrays with superior field electron emission properties, Apl. Mater. 5 (6) (2017) 066102, https://doi.org/10.1063/1.4985107.

[25] K.J. Sankaran, D.Q. Hoang, S. Kunuku, S. Korneychuk, S. Turner, P. Pobedinskas, S. Drijkoningen, M.K. Van Bael, J. D'Haen, J. Verbeeck, K.C. Leou, I.N. Lin, K. Haenen, Enhanced optoelectronic performances of vertically aligned hexagonal boron nitride nanowalls-nanocrystalline diamond heterostructures, Sci. Rep. 6 (March) (2016) 1–11, https://doi.org/10.1038/srep29444. https://doi.org/10.1038/srep29444.

[26] S. Heidger, S. Fries-Carr, J. Weimer, B. Jordan, R. Wu, Dielectric characterization of microwave assisted chemically vapor deposited diamond, in: Proceedings of the IEEE 1998 National Aerospace and Electronics Conference, 1998, pp. 247–254, https://doi.org/10.1109/NAECON.1998.710124.

[27] V. Seshan, D.H. Murthy, A. Castellanos-Gomez, S. Sachdeva, H.A. Ahmad, S.D. Janssens, W. Janssen, K. Haenen, H.S. Van Der Zant, E.J. Sudhölter, T.J. Savenije, L.C. De Smet, Contactless photoconductance study on undoped and doped nanocrystalline diamond films, ACS Appl. Mater. Interfaces 6 (14) (2014) 11368–11375, https://doi.org/10.1021/am501907q.

[28] F. Torrealba-Anzola, A. Chambaudet, J.G. Théobald, M. Jouffroy, C. Jany, F. Foulon, P. Bergonzo, A. Gicquel, A. Tardieu, High frequency photoconductivity of CVD diamond films, Diam. Relat. Mater. 7 (9) (1998) 1338–1341, https://doi.org/10.1016/S0925-9635(98)00200-3.

[29] J.A. Cuenca, E.L.H. Thomas, S. Mandal, D.J. Morgan, F. Lloret, D. Araujo, O.A. Williams, A. Porch, E.L.H. Thomas, S. Mandal, D.J. Morgan, F. Lloret, D. Araujo, O.A. Williams, A. Porch, Microwave permittivity of trace sp^2 carbon impurities in sub-micron diamond powders, ACS Omega 3 (2) (2018) 2183–2192, https://doi.org/10.1021/acsomega.7b02000. https://pubs.acs.org/doi/abs/10.1021/acsomega.7b02000.

[30] J.A. Cuenca, E.L.H. Thomas, S. Mandal, O. Williams, A. Porch, Investigating the broadband microwave absorption of nanodiamond impurities, IEEE Trans. Microw. Theor. Tech. 63 (12) (2015) 4110–4118, https://doi.org/10.1109/TMTT.2015.2495156.

[31] D. Slocombe, A. Porch, E. Bustarret, O. Williams, Microwave properties of nanodiamond particles, Appl. Phys. Lett. 102 (24) (2013) 244102, https://doi.org/10.1063/1.4809823. http://link.aip.org/link/APPLAB/v102/i24/p244102/s1&Agg=doi.

[32] Q. Hu, M. Hirai, R.K. Joshi, A. Kumar, Structural and electrical characteristics of nitrogen-doped nanocrystalline diamond films prepared by CVD, J. Phys. Appl. Phys. 42 (2) (2009) 1–4, https://doi.org/10.1088/0022-3727/42/2/025301.

[33] A. Hoffman, R. Brener, A. Laikhtman, Y. Avigal, P.J. Evans, Enhancement of diamond CVD nucleation on quartz by high dose titanium implantation, Diam. Relat. Mater. 4 (5–6) (1995) 765–769, https://doi.org/10.1016/0925-9635(94)05278-6.

[34] J.A. Cuenca, E.L.H. Thomas, S. Mandal, O.A. Williams, A. Porch, Microwave determination of sp^2 carbon fraction in nanodiamond powders, Carbon 81 (1) (2015) 174–178, https://doi.org/10.1016/j.carbon.2014.09.046. http://linkinghub.elsevier.com/retrieve/pii/S0008622314008987.

[35] D.M. Pozar, Microwave Engineering, fourth ed., Wiley, 2011. https://books.google.co.uk/books?id=JegbAAAAQBAJ.

[36] J.A. Cuenca, S. Klein, R. Ruger, A. Porch, R. Rüger, A. Porch, Microwave complex permeability of magnetite using non-demagnetising and demagnetising cavity modes, in: Microwave Conference (EuMC), 2014 44th European, Rome, 2014, pp. 128–131, https://doi.org/10.1109/EuMC.2014.6986386. http://ieeexplore.ieee.org/xpl/articleDetails.jsp?reload=true&arnumber=6986386.

[37] A. Porch, D. Slocombe, P.P. Edwards, Microwave absorption in powders of small conducting particles for heating applications, Phys. Chem. Chem. Phys. : Phys. Chem. Chem. Phys. 15 (8) (2013) 2757–2763, https://doi.org/10.1039/

c2cp43310a. http://www.ncbi.nlm.nih.gov/pubmed/23321957.

[38] A. Porch, D.I. Odili, P.A. Childs, Microwave characterisation of carbon nanotube powders, Nanoscale research letters 7 (429) (2012) 1—5, https://doi.org/10.1186/1556-276X-7-429. http://www.pubmedcentral.nih.gov/articlerender.fcgi?artid=3432008&tool=pmcentrez&rendertype=abstract.

[39] O.A. Williams, O. Douhéret, M. Daenen, K. Haenen, E. Osawa, M. Takahashi, Enhanced diamond nucleation on monodispersed nanocrystalline diamond, Chem. Phys. Lett. 445 (4—6) (2007) 255—258, https://doi.org/10.1016/j.cplett.2007.07.091.

[40] S. Raina, W.P. Kang, J.L. Davidson, Nitrogen incorporated nanodiamond film with 'ridge' surface morphology for detection of bio-analyte, Diam. Relat. Mater. 18 (2—3) (2009) 574—577, https://doi.org/10.1016/j.diamond.2008.11.016. https://doi.org/10.1016/j.diamond.2008.11.016.

[41] M. Ficek, K.J. Sankaran, J. Ryl, R. Bogdanowicz, I.-N. Lin, K. Haenen, K. Darowicki, Ellipsometric investigation of nitrogen doped diamond thin films grown in microwave $CH_4/H_2/N_2$ plasma enhanced chemical vapor deposition, Appl. Phys. Lett. 108 (24) (2016) 241906, https://doi.org/10.1063/1.4953779. http://aip.scitation.org/doi/10.1063/1.4953779.

[42] V. Mochalin, S. Osswald, Y. Gogotsi, Contribution of functional groups to the Raman spectrum of nanodiamond powders contribution of functional groups to the Raman spectrum of nanodiamond powders, Chem. Mater. 128 (35) (2009) 273—279, https://doi.org/10.1021/cm802057q.

[43] L. Gines, S. Mandal, A.-I. Ahmed, C.-L. Cheng, M. Sow, O. Williams, Positive zeta potential of nanodiamonds, Nanoscale (2017) 12549—12555, https://doi.org/10.1039/C7NR03200E. http://pubs.rsc.org/en/Content/ArticleLanding/2017/NR/C7NR03200E.

[44] F.Y. Xie, W.G. Xie, L. Gong, W.H. Zhang, S.H. Chen, Q.Z. Zhang, J. Chen, Surface characterization on graphitization of nanodiamond powder annealed in nitrogen ambient, Surf. Interface Anal. 42 (9) (2010) 1514—1518, https://doi.org/10.1002/sia.3350.

[45] T.Y. Leung, W.F. Man, P.K. Lim, W.C. Chan, F. Gaspari, S. Zukotynski, Determination of the sp^3/sp^2 ratio of a-C:H by XPS and XAES, J. Non-Cryst. Solids 254 (1—3) (1999) 156—160, https://doi.org/10.1016/S0022-3093(99)00388-9.

[46] M. Aramesh, K. Fox, D.W.M. Lau, J. Fang, K. Ostrikov, S. Prawer, J. Cervenka, Multifunctional three-dimensional nanodiamond-nanoporous alumina nanoarchitectures, Carbon 75 (2014) 452—464, https://doi.org/10.1016/j.carbon.2014.04.025. https://doi.org/10.1016/j.carbon.2014.04.025.